OPTICA

Data encryption with chaotic light in the long wavelength infrared atmospheric window

Pierre Didier,[1,2,*] Sara Zaminga,[1] Olivier Spitz,[1,3] Jiagui Wu,[4] Elie Awwad,[1] Gregory Maisons,[2] and Frederic Grillot[1,5]

[1]LTCI Télécom Paris, Institut Polytechnique de Paris, 19 place Marguerite Perey, Palaiseau, 91120, France
[2]mirSense, Campus Eiffel, Bâtiment E-RDC, 1 rue Jean Rostand, Orsay, 91400, France
[3]Current address: CREOL, College of Optics and Photonics, University of Central Florida, Orlando, Florida 32816, USA
[4]School of Physical Science and Technology, Southwest University, Chongqing 400715, China
[5]Center for High Technology Materials, University of New Mexico, 1313 Goddard SE, Albuquerque, New Mexico 87106, USA
*pierre.didier@telecom-paris.fr

Received 3 November 2023; revised 21 February 2024; accepted 8 March 2024; published 30 April 2024

In environments where traditional fiber optic cables are impractical, free-space optical communications offer a promising solution for transmitting large amounts of data, especially in the mid-infrared wavelength range. Despite the advantages of minimal atmospheric interference and stable signals, the vulnerability of wireless optical communications to eavesdropping poses a significant challenge. This study addresses this challenge by demonstrating a method for privately transmitting optical data using photonic chaos from distributed feedback quantum cascade lasers operating at 9.3 μm. Signal processing techniques are applied to enhance the quality of the transmission over distances exceeding 30 m, accompanied by a comprehensive analysis of the photonic chaos complexity to ensure data confidentiality. These findings mark a significant advancement in developing private communications systems within the thermal atmospheric window, with a substantially reduced risk of interception by adversaries. The research not only contributes to secure communications but also has potential implications for enhancing security of data transmission in challenging environments, impacting various industries and applications.

https://doi.org/10.1364/OPTICA.511171

1. INTRODUCTION

Free-space optics (FSO) is envisioned as a possible solution to close the last-mile gap in peculiar cases where installation, maintenance, and deployment of optical fiber can be prohibitively expensive. Its versatility allows for applications in multihop configurations, making it a practical choice that does not require frequency allocation to complement an existing communications infrastructure. It is worth noting that in specific situations, FSO systems can surpass RF networks in data rates while also offering infrastructure and maintenance advantages compared to the development of fiber networks [1]. Recent results have demonstrated data rates up to Tbits/s at 1.5 μm wavelength [2,3]. However, the mid-infrared (MIR) wavelength range is particularly advantageous for FSO application, especially in the $8-14$ μm range, due to high atmospheric transparency and strong resistance to degraded atmospheric conditions [4], including turbulence [5]. Moreover, the MIR beam is noticeably stealthy in the atmosphere because of the strong thermal black-body radiation. The recent efforts spent on the development of new reliable FSO sources can benefit from cutting-edge mid-infrared light-emitting devices: optical parametric oscillators (OPO) [6], super-continuum generation sources [7], and cascaded lasers [8,9]. Some of those mid-infrared sources have already been proven useful for applications such as spectroscopy [10–12], medicine [13,14], and FSO telecommunications. For the latter, impressive results have been obtained using frequency conversion from a 1.5 μm to 3.4 μm wavelength, with data rates reaching hundreds of Gbit/s [15]; however, these results still suffer from low MIR output power associated with a very high power consumption for the near-infrared pump laser. Concurrently, the cascaded technology constitutes an important step forward for the generation of high output power signals in the mid-infrared. Quantum cascade laser (QCL) technology [8] is now mature, with continuous wave (CW) operation at room temperature. These semiconductor lasers are based on an engineered superlattice heterostructure. The photon emission comes from unipolar intersubband transition, ensuring an ultrafast (order of the picosecond) carrier lifetime [16]. QCLs offer remarkable output power levels reaching up to hundreds of milliwatts in monomode operation [17]. This is of utter relevance as the maximum transmission distance scales with the available optical power and our near-term goal is to increase the propagation distance to achieve free-space communications over hundreds of meters. Consequently, QCLs emerge as the preferred option for telecommunications applications in the MIR domain. For example, a 30 Gbit/s-transmission over a 31-meter link has been demonstrated [18], exploiting QCLs emitting in the $8-14$ μm window, and whose beam was

modulated by a unipolar Stark-effect-based external modulator [19,20]. Also, direct modulation transmission is promising for reaching tens of Gbit/s data rates [21]. Despite these copious benefits, physical-layer security was not thoroughly addressed in MIR free-space communications. Yet, the increasing release of sensitive information and the consistent threat of cybercrime compel the research to investigate ingenious alternatives to provide data security. The application of private FSO systems can span across various sectors, including military, banking, and civilian uses.

Among the methods that have been studied to enable secure FSO communications, quantum key distribution (QKD) has attracted much attention owing to the high level of protection provided by the intrinsic properties of photon entanglement. Yet, FSO QKD is still hindered by expensive transmission/reception apparatus [22] while government agencies such as the American National Security Agency (NSA) and the British National Cyber Security Centre (NCSC) have raised concerns about real-field applications of QKD systems [23]. A recent FSO QKD study demonstrated that effective entanglement can be maintained for successful transmission of up to one hundred bits per second over a distance of 10 kilometers between ground-to-ground stations. Interestingly, the losses incurred by the link in an urban environment were estimated to be similar to those experienced during communications with a low space orbit satellite. However, latest findings reveal that communication is highly sensitive to degraded atmospheric conditions, especially in the presence of rain [24]. QKD technologies are not yet available at MIR wavelengths due to the lack of efficient single-photon detectors and efficient sources. Using the chaos synchronization of coupled lasers for ciphering sensitive message is a promising approach in the field of free-space optical private communications [25–27]. Indeed, complex chaotic dynamics are very interesting to guarantee a fast-decaying autocorrelation function for the time-dependent fluctuations in the laser's output, and this is associated with a high unpredictability of the transmitted message. With this protocol, a message is embedded within a chaotic carrier at the emitter side. The deciphering of the message is achieved thanks to chaos synchronization of a similar second laser at the receiver side, and by computing the difference between the synchronized output of the receiver and the transmitted signal [28]. Applications of private FSO communications usually aim for data rates in the hundreds of Mbit/s ranges while ensuring high security, stealthiness, and straightforward implementation. A real-field application of a 2.4 Gbit/s chaos-based private transmission was demonstrated in the near-infrared domain, at 1.55 μm over the 120-km fiber network of the metropolitan area of Athens, Greece [29]. However, the exploitation of both widespread fiber medium and commercial laser diodes limits the application relevance and data integrity, as the fixed fiber system can be discretely probed for an extensive time and some information may be eavesdropped. Conversely, free-space communication is intrinsically apt for this method because it can offer a mobile platform, which is much more complex for the eavesdropper to probe and yet allows precise acquisition and tracking for the legitimate receiver, as underlined in a transmission experiment between two transiting ships separated by several kilometers [30]. In this direction, intersubband mid-infrared technology is an elective choice because it does not exhibit a relaxation oscillation frequency [31], which is a common limitation for nonlinear dynamics bandwidths [32]. Simulations show the possibility to generate broadband chaos with QCLs [33]; related experiments, however, have not yet demonstrated this feature. To the best of our knowledge, the maximum chaos bandwidth is limited to tens of MHz [34]. A chaos-based communications between unidirectionally coupled 5.6-μm QCLs has been achieved at a data rate of 0.5 Mbit/s over a distance of 1 m [35]. Unfortunately, in this proof-of-concept experiment, the emission wavelength was not within the thermal atmospheric window, making a long-distance implementation impractical.

In this work, we achieve an 8 Mbit/s chaos-based private transmission between two coupled distributed-feedback (DFB) QCLs emitting at 9.3 μm. The specific wavelength under consideration offers a compelling combination of low detectability due to thermal noise and enhanced security through chaos. As a result, this wavelength is particularly well-suited for private communications applications that prioritize message protection over high data rates, such as tactical links in naval environments [30]. The communications quality is assessed through bit-error-rate (BER) measurements and eye diagrams. The generated chaos has been characterized with various tools for the proof of highly complex traces, guaranteeing the unpredictability of the transmitted signal: Lyapunov exponents (LEs), strange attractors, and correlation integrals [36] have been extracted as parameters of paramount importance. The synchronization and anti-synchronization properties of the employed sources are estimated through statistical means, i.e., auto-correlation and cross-correlation.

2. GENERATION OF CHAOTIC NONLINEAR DYNAMICS IN THE DFB QCL

A. Experimental Setup

Figure 1 shows the experimental setup: The transmitter is constituted by a CW room-temperature DFB QCL (named ML) emitting at 9.3 μm. The ML is biased with a DC current low-noise source (Wavelength Electronics, QCL lab 2000) and alternatively modulated electrically with a waveform generator (Agilent, 33522B), through a bias tee. Both QCLs are housed in a ILX sealed mount for extensive temperature control and the laser's beam is collimated by a lens with a short focal length. A Peltier cooler guarantees a constant temperature. The two QCLs were designed and manufactured by mirSense, ensuring a special attention to their similarity. The dimension of the two QCLs is a 6 μm wide × 2 mm long buried structure. The QCLs were grown by molecular beam epitaxy (MBE) on an InP substrate. The active region of the lasers consists of GAInAs electron barriers and AlInAs quantum wells, and is designed using a two-phonon-resonant heterostructure. Additionally, the lasers have a top metal surface grating for monomode emission and a high reflective back facet to minimize losses [37]. In continuous wave operation, the QCL emits 25 mW for a current of 400 mA and a voltage of around 10 V, as shown in Fig. 2(a). Additional details regarding the SL's wavelength emission can be found in Fig. S1 of Supplement 1. The ML is driven chaotically by self-optical feedback coming from an external cavity mirror. The intensity of optical feedback is tuned by a MIR polarizer as the optical emission of QCLs is TM polarized. The cavity length was set to approximately 20 cm. To protect the master QCL from back reflections and from the influence of the slave laser, we used an MIR optical isolator. The signal then propagates in free space for either a 2 m or 31 m distance, in the case where the Herriott cell is in place. The receiver (designated as SL) is matched with the ML, presenting the same design geometry. The emitting wavelength is perfectly matched with that of

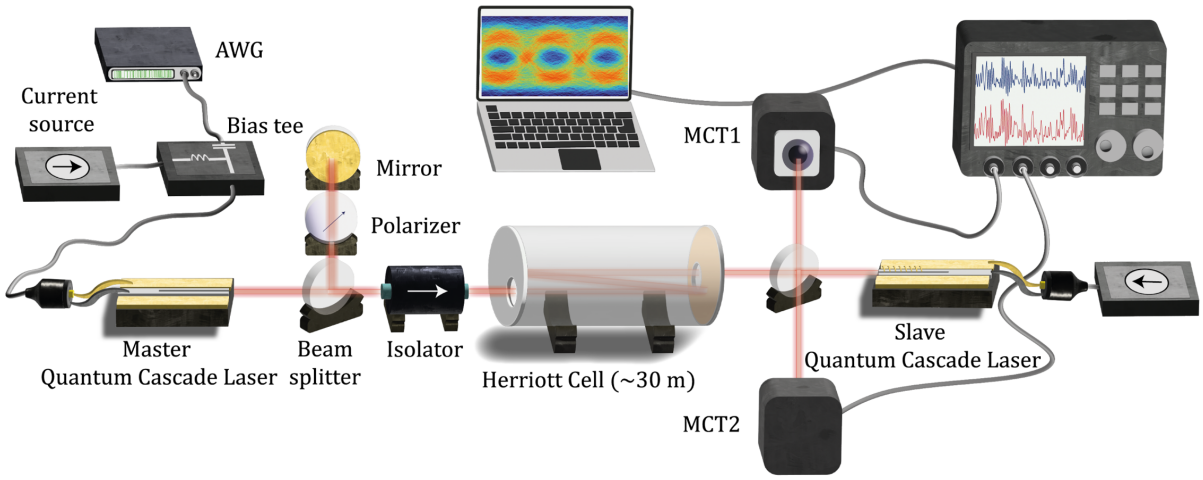

Fig. 1. Schematic of the experimental setup. A 9.3 μm wavelength CW DFB QCL (Master Laser, ML) emits around 30 mW of optical power and is in an external optical feedback (EOF) configuration to generate photonic chaos. An arbitrary waveform generator (AWG) electrically modulates the QCL with a pseudo-random binary sequence (PRBS) on–off keying (OOK) modulation with a small amplitude (< 10 mV). The transmitted beam goes to the receiver side through an optical isolator, avoiding back-coupling reflections. The path length can be adjusted from a 2 m to a 31 m configuration using a Herriott cell that was left open and subsequently filled with ambient air. The transmitted signal is injected into a second QCL (Slave Laser, SL), which is chaos-synchronized with the emitter. Two 700 MHz 3 dB bandwidth mercury cadmium telluride (MCT) detectors collect the master and the slave signals, processed by a custom MATLAB program to retrieve the hidden message.

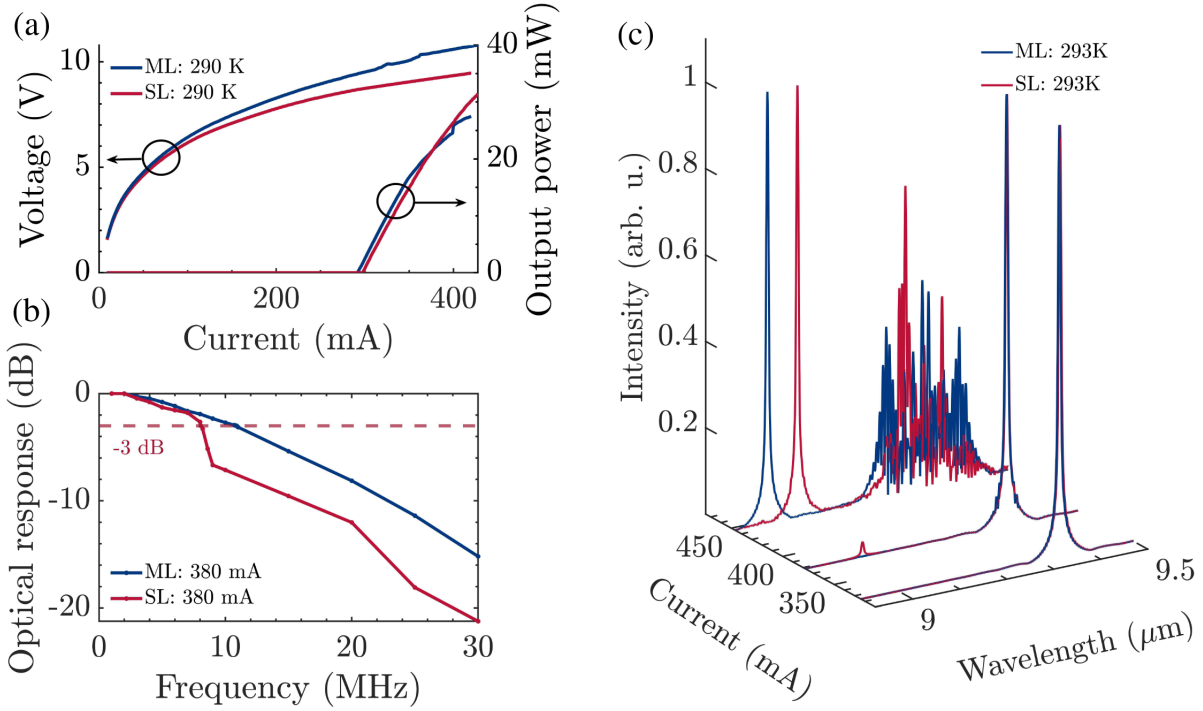

Fig. 2. 9.3 μm Distributed-feedback quantum cascade laser characterization. (a) Light intensity voltage (LIV) of the two DFB-QCLs: master laser (ML) and the slave laser (SL) at 290 K. The two LIV curves are very similar, showing the matching geometry. (b) Optical responses of the electrically modulated ML and SL at a current of 380 mA and a temperature around 283 K. The bandwidths of the master and the slave laser are 10 MHz and 7 MHz, respectively. The QCL's bandwidth constraint arises from the presence of numerous electrical wires leading to a high-impedance device. (c) Optical spectrum of the ML and the SL. The two QCLs are DFB up to 380 mA and show a near perfectly matched emission wavelength. For higher current, the two QCLs become highly multimode as a result of the competition between modes and a nonuniform widening of the gain, specifically corresponding to the Fabry–Perot modes.

the master laser for bias currents below 400 mA [Fig. 2(c)]. This condition is as arduous as fundamental: Theoretically, close physical parameters are necessary for good synchronization; however, process variations during the fabrication cause a mismatch of the lasers' characteristics, even when taken as close as possible from the same wafer. Figure 2(a) highlights the deviations in terms of the electrical properties in the light intensity voltage (LIV) curves. By using a beam splitter at the legitimate receiver side, one can simultaneously recover the signal from the master and the signal from the slave with two 700 MHz bandwidth mercure cadmium

telluride (MCT) detectors. While having a relatively high cost, MCTs offer the benefit of a substantial 3 dB bandwidth coupled with substantial responsivity. Electrical data resulting from the conversion of the optical signal by the MCT detectors are recorded by a real time oscilloscope (Tektronix, MSO44). The sampling rate is set to 250 MS/s, chosen to provide precise resolution without excessive oversampling of the electrical signals, particularly when their primary frequency components are below 40 MHz.

B. Chaos Synchronization: Master–Slave Configuration

We performed a chaos synchronization quality evaluation as shown in Fig. 3. The chaos synchronization is obtained by injecting the QCL master signal into the slave QCL cavity for which the injection locking condition is satisfied [38]. The open loop configuration (or, in other words, the absence of feedback mirror for the slave QCL) means that the receiver laser is driven chaotic only if it is injected with the transmitted signal [39,40]. The practicability and ease of the setup, the possibility to neglect the phase-matching parameters [41] of the feedback and the efficiency of chaos synchronization made the open-loop configuration the preferred choice. The chaos synchronization efficiency is ensured by a proper setting of the operating current and temperature for both lasers, to match their emission wavelengths. As a first attempt before selecting relevant current/temperature values, an operating point is chosen by electrically modulating the pump current of the master with a 200 mV amplitude, 100 kHz frequency sinusoidal waveform. In fact, the master current modulation leads to a modulation of its emission wavelength as well, as evinced from Fig. 3(a). The slave laser, in response to the injection, exhibits periodic intensity peaks when the wavelengths of the two lasers overlap. This behavior enables us to accurately align the optics between the master and slave lasers. Moreover, precise setting of the operating current and temperature of both sources is crucial to complete effective chaos synchronization. Next, we evaluate the optimal current value that enables the synchronization (or anti-synchronization) of the two lasers. The continuous wave operation is maintained for both lasers, with the slave laser bias gradually varied from the laser threshold up to 410 mA, while the master laser bias remains fixed at 370 mA. The choice of the master current value is based on the observation of relevant chaotic dynamics in the laser output at that particular current spot. Sweeping the current of the slave laser leads to three equidistant injection locking ranges, as shown in Fig. 3(b). In fact, when injecting the slave with the master beam, its suppressed side modes can be consequently excited [35]. The first interval is found right above the laser threshold (290 mA). The others are located, respectively, around 350 mA and 400 mA, accounting for a separation of about 50 mA with respect to one another. The blue and orange colors in Fig. 3(b) mark, respectively, synchronization ranges and anti-synchronization ones, evidencing a shift from one to the other by simply tuning the slave QCL current of some fractions of mA, as it has already been observed in a previous study of conventional semiconductor lasers [42]. Each injection locking range shows the two types of synchronization, with a drop of the cross-correlation (CC) coefficient in correspondence to the turning point. Around 290 mA, the maximum cross-correlation coefficient is 97%, and slightly smaller values are reached around 350 mA. The width of the injection locking interval diminishes, though. When the slave bias exceeds 380 mA, the transition to a multimode operation, as illustrated in Fig. 2(c) and Fig. S1 of Supplement 1, may be the reason for the observed

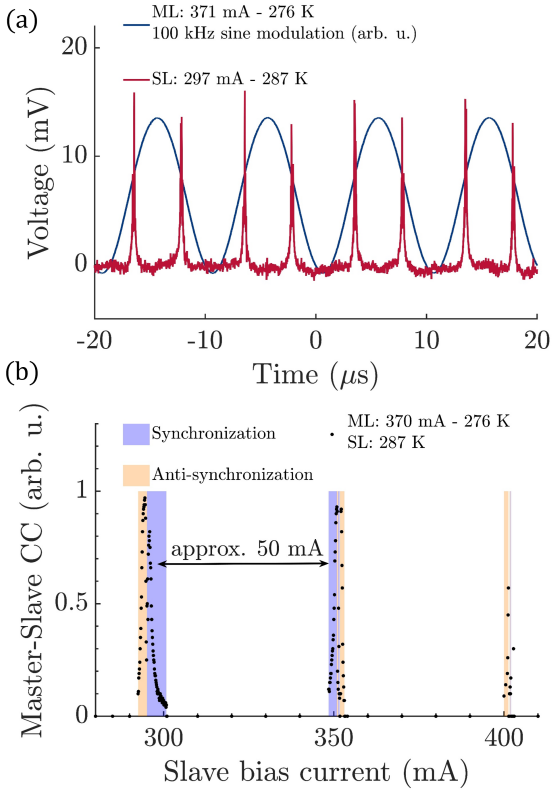

Fig. 3. Injection in the slave laser. (a) ML (blue) and SL (red) time-traces during tentative injection locking when the master QCL is electrically modulated. The ML is biased at 371 mA at 276 K. The SL is biased at 297 mA at 287 K. The SL response peaks indicate the efficiency of the injection of the QCLs' carrier frequencies. (b) Experimental data (black dots) representing the maximum of the master–slave cross correlation (CC) as a function of the slave bias current. The synchronization intervals are marked in blue, and the anti-synchronization ones are marked in orange. The master operating point is 370 mA at 276 K. The slave operating point is 287 K, with a bias current sweeping from 290 mA (just above threshold current) to 410 mA.

55% cross-correlation value, leading to a lower synchronization quality.

3. PRIVATE COMMUNICATION PERFORMANCE EVALUATION

Details about the algorithms used for the message recovery and system performance evaluation are provided in Fig. S5 of Supplement 1. The successful private transmissions were obtained in an anti-synchronization configuration, independently of the enciphered message data rate and amplitude. The study examined two configurations: the two-meter propagation setup and propagation through a 31 m Herriott cell. Figures 4(a) and 4(d) display, after appropriate filtering and normalization, in blue the master signal, in red the slave signal, in green the original message and in purple the difference signal, respectively. The message is a non-return-to-zero (NRZ) pseudo-random binary sequence (PRBS) with a length of 2^7-1 and an amplitude of modulation varying from 2 to 10 mV. Figures 4(b) and 4(e) illustrate the 1D auto-correlation and cross-correlation, for two different data rates. By utilizing a 127-bit sequence repetition, the presence of this repetition

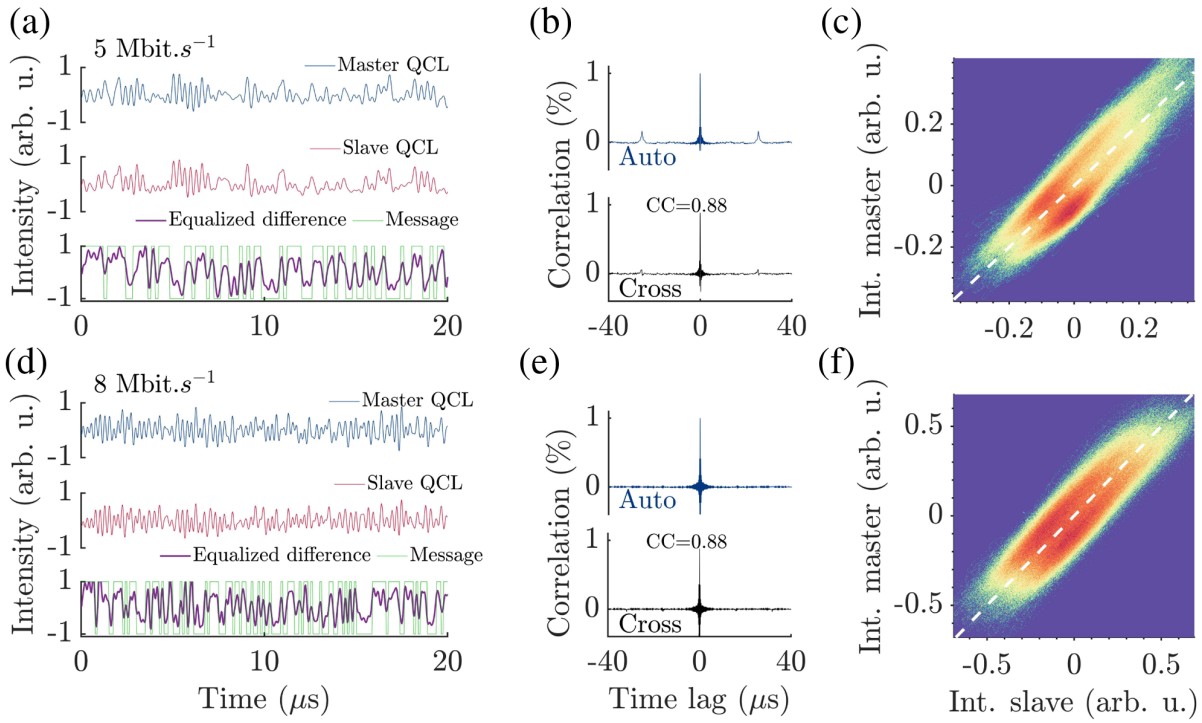

Fig. 4. Chaotic anti-synchronization in the master-slave configuration. (a) Experimental timetraces for the 5 Mbit/s transmission: (blue) master signal, (red) inverted slave signal, (green) original message, (purple) equalized difference. (b) Auto-correlation (master only) and cross-correlation diagrams for the filtered intensity of the slave and the master QCLs. (c) 2D correlation diagram for the intensity of the ML (y axis) and SL (x axis). The signal of the slave is flipped to have a positive correlation. (d)–(f) Graphs represent the same information as the graphs (a)–(c), respectively, but at a data rate of 8 Mbit/s.

could be observed in the auto-correlation diagram through the appearance of side peaks in the master signal. Specifically, at a transmission rate of 5 Mbit/s, only two side peaks with low amplitude levels (<15%) are evident. However, at an 8 Mbit/s transmission rate, the presence of a single narrow main lobe at a nearly zero time lag serves as a reliable indicator of a very low signal-to-chaos ratio, signifying an effective enciphering of the PRBS signal. However, in a real transmission, the bit patterns will not be as obviously repetitive. To estimate the synchronization quality between the master and the slave signal, the cross-correlation between the master and the slave are computed as a function of the lag between the time traces. A higher maximum value in the cross-correlation indicates better synchronization quality. Figures 4(c) and 4(f) depict the 2D correlation heatmap (that is, the master intensity versus the slave intensity). A good synchronization is accompanied by a straight line with a positive slope of 45° in the case of synchronization. To account for anti-synchronization, the intensity of the slave laser is flipped so that the white dashed line, indicating the trend, has a positive slope.

To measure the transmission efficiency, the bit error rate (BER) is evaluated and is defined as the ratio of bit errors over the number of sent bits. It is fundamental to keep this value as low as possible, to have an effective communication. Forward-error-correction (FEC) coding and decoding can be implemented to correct bit errors by introducing redundancy. Hence, an FEC overhead should be taken into account in the sizing of the transmission system. In our case, we chose a maximum tolerated pre-FEC BER of 4%, corresponding to a FEC code with 27% overhead and hard-decision (HD) decoding [43]. With those requirements, we were able to achieve error-free communication. This high BER condition will introduce some latency and more burdensome processing, but the aimed application is not severely influenced [44]. Table 1 highlights cross-correlation coefficients as high as 88% for the 8 Mbit/s configuration. Unfortunately, higher data rates were impossible to achieve because of the restrained electrical modulation bandwidth of the master QCL, resulting in an unacceptable BER up to 8%. To determine the privacy of transmission, one should also consider the capability to recover the message for an eavesdropper intercepting the signal coming from the transmitted beam. When considering the best-matching filtering (the one utilized to present the timetraces in Figs. 4(a) and 4(d) for both 5 and 8 Mbit/s data rates), the eavesdropper would achieve a BER of approximately 42.9% and 41.3%, respectively. The lower limit commonly accepted for a nondecipherable transmission is around 25% [45]; hence, the privacy of the transmission is granted.

Table 1. Main Private Transmission Experimental Results[a]

Data Rate	CC	Master BER	Difference BER
1 Mbit/s (Herriott cell)	50%	25.4%	4.1%
5 Mbit/s	88%	42.9%	1.4%
8 Mbit/s	88%	41.3%	2.5%

[a]The following results can be found in Figs. 5 and 6. Herriott cell (HC) corresponds to the configuration with the multipass cell, increasing the free-space path between the ML and SL to 31 m instead of 2 m.

The eye diagram in Fig. 5 is used to verify the quality of the signal transmission. It is obtained as the superposition of all the sent bits (which corresponds to approximately 50 kbits for 8 Mbit/s) on the same time interval, equal to two symbol time slots. As for the BER, the eye diagram is visualized for both the master signal and the difference signal for two different data rates: 5 Mbit/s and 8 Mbit/s. The eavesdropper is deemed to be in the best-matching

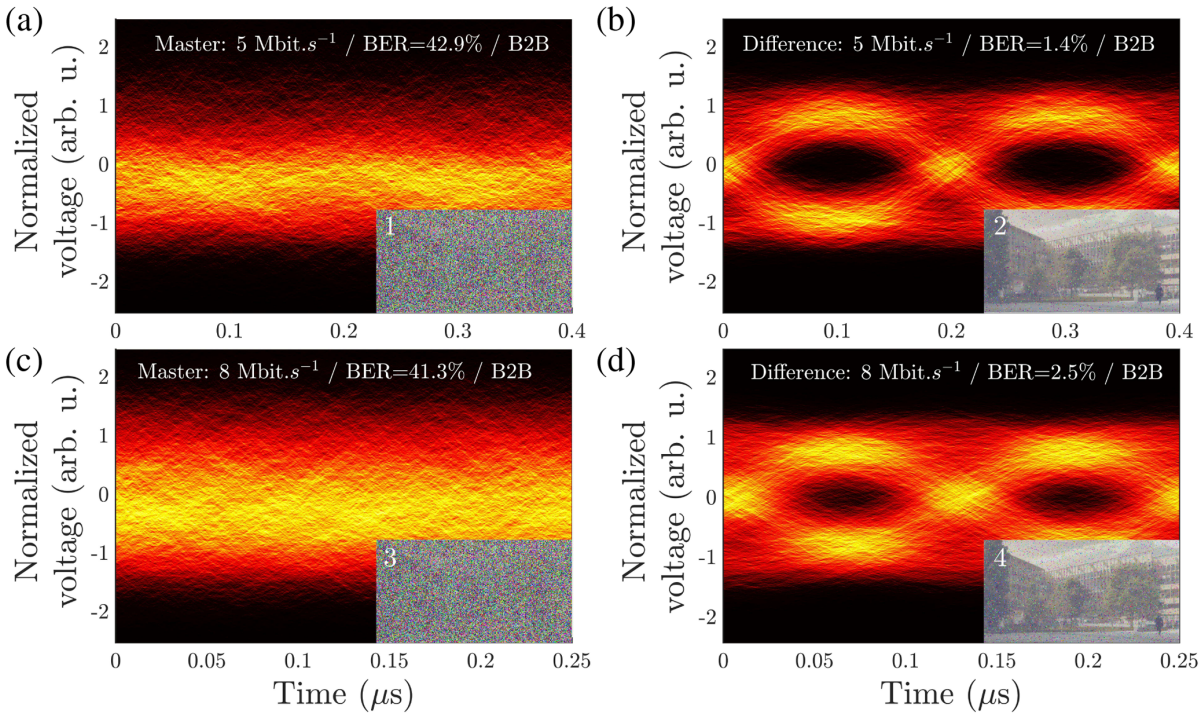

Fig. 5. Private transmission using chaos synchronization. Eye diagrams of the transmission after a free-space propagation of approximately 2 m. Eye diagram is the overlapping of the recorded signal at a fixed time interval corresponding to an integer multiple of the bit time length. This tool enables a qualitative evaluation of the transmission performance. A low error rate is equivalent to an open eye, indicating the ability to distinguish the various modulation levels. Eye diagram for 5 Mbit/s transmission: (a) Master signal exhibiting an error rate of 42.9% and (b) Difference signal exhibiting an error rate of 1.4%. Eye diagram for 8 Mbit/s transmission: (c) Master signal exhibiting an error rate of 41.3% and (d) Difference signal exhibiting an error rate of 2.5%. The insets 1, 2, 3, and 4 correspond to the recovered image when considering the BER of the transmission.

filtering configuration, which is an extremely unlikely configuration, as it implies that the eavesdropper knows the exact data rate of the enciphered message as well as the coding format (NRZ in our case). From Figs. 5(a) and 5(c), the signal directly retrieved at the receiver end, after digital processing and equalization, is absolutely not decipherable. Meanwhile, the legitimate receiver [Figs. 5(b) and 5(d)] benefits from a low BER ($< 4\%$), which allows an error-free transmission to be achieved after FEC correction, as already mentioned, or even a decipherable picture without error-code correction, as emphasized by the insets. It is important to note that the BER could be even decreased using advanced processing methods. In our study, we implemented feed-forward equalization (FFE), but it had limitations with a changing channel due to the FSO propagation and synchronization quality. In the future, we will be incorporating decision feedback equalization (DFE) to improve the transmission quality. In cases with well-developed chaos, we can further increase the voltage of the modulated message to achieve a low BER for the legitimate user, making it compatible with a lower-threshold FEC code. Indeed, in Fig. S7 of Supplement 1, when the signal-to-chaos ratio is very high, as seen in the 8 Mbit/s transmission (depicted in blue), we have the opportunity to significantly increase the modulation voltage without affecting the concealment of the transmission. This will then substantially decrease the BER of the legitimate user while not compromising the security of the message. Higher data rates are not considered here because of the bandwidth limitation. For the sake of visualization, the insets 1–4 of Figs. 5(a)–5(d) display the results of the attempted private transmission. The information encoded in each pixel is converted into a bit stream, representing the transmitted message. At the receiver end, the retrieved bit stream is transformed back again into an image format. For both data rates, the image remains imperceptible to an eavesdropper who directly detects the laser signal, as demonstrated in Inset 1 and 3 of Figs. 5(a) and 5(c), highlighting the effective containment of the information. When we analyze the difference signal [Figs. 5(b) and 5(d)], the low BER allows for the successful recovery and visualization of the image content in both cases.

Finally, some considerations may be proposed regarding the challenges faced by an eavesdropper in the aimed ground-to-ground communications application: First and foremost, the localization of the transmitted beam in free space has many hurdles; in fact, the divergence at these MIR wavelengths is lower than that at radio frequencies. Moreover, a 9.3 μm wavelength resides in a portion of the electromagnetic spectrum where the thermal atmospheric radiation is at its highest value, which complicates the interception even more. Having said that, assuming that the eavesdropper can still detect the signal, there would be two ways in which it could proceed to decipher the hidden message. The first possibility would be to directly process the chaotic signal to recover the enciphered message. As shown in Fig. S2 of Supplement 1, we assessed the complexity of the chaos generated during the 8 Mbit/s private transmission, extracting multiple positive Lyapunov Exponent (LE) values at $LE_1 \approx 23\ \mu s^{-1}$, $LE_2 \approx 14\ \mu s^{-1}$, $LE_3 \approx 7\ \mu s^{-1}$, $LE_4 \approx 0.7\ \mu s^{-1}$, and $LE_5 \approx -6.2\ \mu s^{-1}$. In agreement with those values, the estimated correlation dimension D_2 is found to be 6. The correlation dimension D_2 is indicative of the fractal dimensionality of the chaotic topological structure [46]. Those criteria illustrate the significant complexity of the

generated photonic chaos in our system, ensuring a high level of unpredictability and rendering the eavesdropper's task extremely resource-intensive. In addition, the signal-to-chaos ratio is very small ($< 1/50$ in our case, whereas $< 1/10$ is a stringent requirement for chaos-based communications [47]), which makes it impossible to decipher with a traditional signal processing method. Nevertheless, advanced methods on chaos analysis can be developed, but their analysis is out of the scope of this paper. The second option for the eavesdropper is to fabricate and process its own QCL without having information on the transmitter source, but solely on the emitted and transmitted signals. The laser would need to have a very close emission wavelength, a matched chaos bandwidth, and a nearly identical geometry to synchronize with the master laser. If this is not guaranteed, only a partial synchronization can be achievable, resulting in the impossibility of an effective message recovery. As aforementioned, the temperature and the current are subject to very fine tuning (mA) to achieve good correlation between the master and the slave.

To extend the free-space transmission path, we used a Herriott cell, which is a cavity consisting of two mirrors facing each other that allowed the beam to bounce back and forth 80 times before exiting; this is equivalent to a 31 m propagation. Despite the introduction of additional optical losses, these losses were limited to 3 dB, primarily attributed to the highly reflective coatings on the mirrors, which achieved a reflectivity of over 99% at the wavelength of operation. To ensure high-quality beam output after this HC, we included an additional telescope before the multipass cell to shape the beam. With this configuration, we achieved a private transmission rate of 1 Mbit/s, while maintaining a low bit error rate (BER) of around 4% for the intended receiver [Fig. 6(a)] and a high BER of around 25% for potential eavesdroppers [Fig. 6(b)]. Additional findings about optimal conditions of operation to ensure privacy are available in Supplement 1 (Fig. S7).

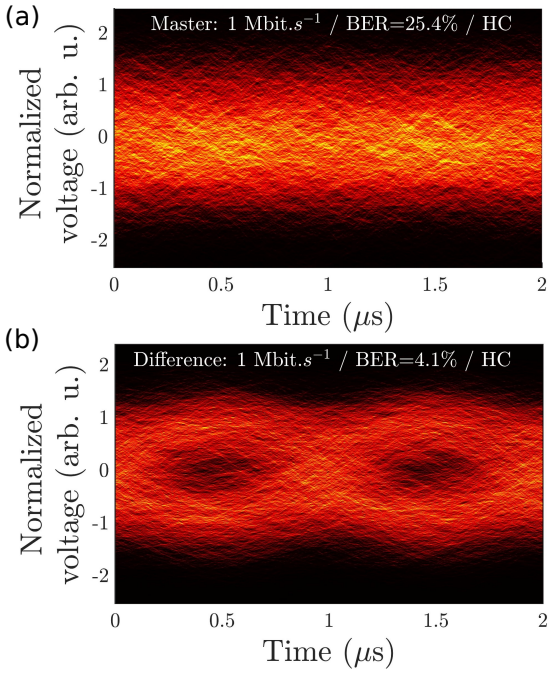

Fig. 6. Eye diagram for the 1 Mbit/s link through the Herriott cell (HC), which is equivalent to a 31 m propagation: (a) Master signal exhibiting an error rate of 25.4% and (b) Difference signal exhibiting an error rate of 4.1%.

4. CONCLUSION

We demonstrated free-space private communications in the long wavelength infrared window at 9.3 μm, with the additional implementation of digital signal processing steps to improve the message recovery. The successful results derived from the insertion of the Herriott cell in the experimental setup envision the attainability of a long-distance private communications in the mid-infrared, such as in between ground stations and vessels in tactical links, where a high data rate is not mandatory. Future investigations will focus on other methods to further tune the nonlinear dynamics in QCLs, for instance with cross-polarization reinjection [48] and filtered feedback [49]. Also, we will study the influence of the QCL geometry on the chaos complexity and bandwidth. Furthermore, in the other transparency window of the mid-infrared band, between 3−5 μm, a valid alternative is constituted by interband cascade lasers (ICLs) exhibiting broader chaos bandwidth than QCLs [50]. Currently, ICLs are limited in terms of the optical power. Finally, further analysis might consider chaos and synchronization in phased-array QCLs with a Talbot-based cavity [51–53], to improve the chaos bandwidth, by modulating the multiple transmitter QCLs with different message signals.

Funding. European Office of Aerospace Research and Development (FA8655-22-1-7032); Direction Générale de l'Armement; Agence Nationale de la Recherche.

Acknowledgment. Direction Générale de l'Armement (DGA), CalQ, and Optopirat projects are supported by the French National Research Agency (ANR) and the European Office for Scientific Research (AFOSR) under grant FA8655-22-1-7032.

Disclosures. The authors declare no competing interests.

Data availability. Data underlying the results presented in this paper are not publicly available at this time but may be obtained from the authors upon reasonable request.

Supplemental document. See Supplement 1 for supporting content.

REFERENCES

1. A. Trichili, M. A. Cox, B. S. Ooi, *et al.*, "Roadmap to free space optics," J. Opt. Soc. Am. B **37**, A184–A201 (2020).
2. E. Ciaramella, Y. Arimoto, G. Contestabile, *et al.*, "1.28 terabit/s (32×40 Gbit/s) WDM transmission system for free space optical communications," IEEE J. Sel. Areas Commun. **27**, 1639–1645 (2009).
3. Y. Horst, B. I. Bitachon, L. Kulmer, *et al.*, "Tbit/s line-rate satellite feeder links enabled by coherent modulation and full-adaptive optics," Light Sci. Appl. **12**, 153 (2023).
4. P. Corrigan, R. Martini, E. A. Whittaker, *et al.*, "Quantum cascade lasers and the Kruse model in free space optical communication," Opt. Express **17**, 4355–4359 (2009).
5. J. J. Liu, B. L. Stann, K. K. Klett, *et al.*, "Mid and long-wave infrared free-space optical communication," Proc. SPIE **11133**, 1113302 (2019).
6. B. Cole, L. Goldberg, S. Chinn, *et al.*, "Compact and efficient mid-IR OPO source pumped by a passively Q-switched Tm: YAP laser," Opt. Lett. **43**, 1099–1102 (2018).
7. M. Montesinos-Ballester, C. Lafforgue, J. Frigerio, *et al.*, "On-chip mid-infrared supercontinuum generation from 3 to 13 μm wavelength," ACS Photon. **7**, 3423–3429 (2020).
8. J. Faist, F. Capasso, D. L. Sivco, *et al.*, "Quantum cascade laser," Science **264**, 553–556 (1994).
9. R. Q. Yang, "Infrared laser based on intersubband transitions in quantum wells," Superlattices Microstruct. **17**, 77–83 (1995).
10. Z. Zhang, T. Gardiner, and D. T. Reid, "Mid-infrared dual-comb spectroscopy with an optical parametric oscillator," Opt. Lett. **38**, 3148–3150 (2013).
11. L. Zhang, G. Tian, J. Li, *et al.*, "Applications of absorption spectroscopy using quantum cascade lasers," Appl. Spectrosc. **68**, 1095–1107 (2014).

12. R. Krebbers, N. Liu, K. Jahromi, *et al.*, "Mid-infrared supercontinuum-based Fourier transform spectroscopy for plasma analysis," Sci. Rep. **12**, 9642 (2022).
13. T. H. Risby and F. K. Tittel, "Current status of midinfrared quantum and interband cascade lasers for clinical breath analysis," Opt. Eng. **49**, 111123 (2010).
14. M. A. Mackanos, D. M. Simanovskii, C. H. Contag, *et al.*, "Comparing an optical parametric oscillator (OPO) as a viable alternative for mid-infrared tissue ablation with a free electron laser (FEL)," Lasers Med. Sci. **27**, 1213–1223 (2012).
15. K. Zou, K. Pang, H. Song, *et al.*, "High-capacity free-space optical communications using wavelength-and mode-division-multiplexing in the mid-infrared region," Nat. Commun. **13**, 7662 (2022).
16. R. Ferreira and G. Bastard, "Evaluation of some scattering times for electrons in unbiased and biased single- and multiple-quantum-well structures," Phys. Rev. B **40**, 1074–1086 (1989).
17. Y.-J. Guan, X.-F. Jia, S.-S. Li, *et al.*, "High power tapered sampling grating distributed feedback quantum cascade lasers," IEEE Photon. Technol. Lett. **32**, 305–308 (2020).
18. P. Didier, H. Dely, T. Bonazzi, *et al.*, "High-capacity free-space optical link in the midinfrared thermal atmospheric windows using unipolar quantum devices," Adv. Photon. **4**, 056004 (2022).
19. F. Capasso, C. Sirtori, and A. Y. Cho, "Coupled quantum well semiconductors with giant electric field tunable nonlinear optical properties in the infrared," IEEE J. Quantum Electron. **30**, 1313–1326 (1994).
20. H. Dely, T. Bonazzi, O. Spitz, *et al.*, "10 Gbits^{-1} free space data transmission at 9 μm wavelength with unipolar quantum optoelectronics," Laser Photon. Rev. **16**, 2100414 (2022).
21. X. Pang, H. Dely, R. Schatz, *et al.*, "Gb/s LWIR FSO transmission at 9.6 μm using a directly-modulated quantum cascade laser and an uncooled quantum cascade detector," in *Optical Fiber Communication Conference (OFC)*, 2022, S. Matsuo, D. Plant, J. Shan Wey, C. Fludger, R. Ryf, and D. Simeonidou, eds., Technical Digest Series (Optica Publishing Group, 2022), paper Th4B.5.
22. E. Diamanti, H.-K. Lo, B. Qi, *et al.*, "Practical challenges in quantum key distribution," npj Quantum Inf. **2**, 1–12 (2016).
23. W. Luo, L. Cao, Y. Shi, *et al.*, "Recent progress in quantum photonic chips for quantum communication and internet," Light Sci. Appl. **12**, 175 (2023).
24. L. Bulla, M. Pivoluska, K. Hjorth, *et al.*, "Nonlocal temporal interferometry for highly resilient free-space quantum communication," Phys. Rev. X **13**, 021001 (2023).
25. G. D. Vanwiggeren and R. Roy, "Communication with chaotic lasers," Science **279**, 1198–1200 (1998).
26. P. Colet and R. Roy, "Digital communication with synchronized chaotic lasers," Opt. Lett. **19**, 2056–2058 (1994).
27. S. Sivaprakasam and K. A. Shore, "Demonstration of optical synchronization of chaotic external-cavity laser diodes," Opt. Lett. **24**, 466–468 (1999).
28. A. Sanchez-Diaz, C. R. Mirasso, P. Colet, *et al.*, "Encoded Gbit/s digital communications with synchronized chaotic semiconductor lasers," IEEE J. Quantum Electron. **35**, 292–297 (1999).
29. A. Argyris, D. Syvridis, L. Larger, *et al.*, "Chaos-based communications at high bit rates using commercial fibre-optic links," Nature **438**, 343–346 (2005).
30. W. Rabinovich, C. Moore, H. Burris, *et al.*, "Free space optical communications research at the U.S. Naval Research Laboratory," Proc. SPIE **7587**, 9–23 (2010).
31. R. Paiella, R. Martini, F. Capasso, *et al.*, "High-frequency modulation without the relaxation oscillation resonance in quantum cascade lasers," Appl. Phys. Lett. **79**, 2526–2528 (2001).
32. J. Mørk, J. Mark, and B. Tromborg, "Route to chaos and competition between relaxation oscillations for a semiconductor laser with optical feedback," Phys. Rev. Lett. **65**, 1999–2002 (1990).
33. C. Chen, Z. Jia, Y. Lv, *et al.*, "Broadband laser chaos generation using a quantum cascade laser with optical feedback," Opt. Lett. **46**, 5039–5042 (2021).
34. L. Jumpertz, K. Schires, M. Carras, *et al.*, "Chaotic light at mid-infrared wavelength," Light Sci. Appl. **5**, e16088 (2016).
35. O. Spitz, A. Herdt, J. Wu, *et al.*, "Private communication with quantum cascade laser photonic chaos," Nat. Commun. **12**, 3327 (2021).
36. J. Wu, S.-W. Huang, Y. Huang, *et al.*, "Mesoscopic chaos mediated by Drude electron-hole plasma in silicon optomechanical oscillators," Nat. Commun. **8**, 15570 (2017).
37. M. Carras, G. Maisons, B. Simozrag, *et al.*, "Room-temperature continuous-wave metal grating distributed feedback quantum cascade lasers," Appl. Phys. Lett. **96**, 161105 (2010).
38. S. Boccaletti, L. M. Pecora, and A. Pelaez, "Unifying framework for synchronization of coupled dynamical systems," Phys. Rev. E **63**, 066219 (2001).
39. R. Vicente, T. Pérez, and C. R. Mirasso, "Open-versus closed-loop performance of synchronized chaotic external-cavity semiconductor lasers," IEEE J. Quantum Electron. **38**, 1197–1204 (2002).
40. M. W. Lee, J. Paul, S. Sivaprakasam, *et al.*, "Comparison of closed-loop and open-loop feedback schemes of message decoding using chaotic laser diodes," Opt. Lett. **28**, 2168–2170 (2003).
41. M. Peil, T. Heil, I. Fischer, *et al.*, "Synchronization of chaotic semiconductor laser systems: a vectorial coupling-dependent scenario," Phys. Rev. Lett. **88**, 174101 (2002).
42. I. Wedekind and U. Parlitz, "Experimental observation of synchronization and anti-synchronization of chaotic low-frequency-fluctuations in external cavity semiconductor lasers," Int. J. Bifurcation Chaos **11**, 1141–1147 (2001).
43. F. Chang, K. Onohara, and T. Mizuochi, "Forward error correction for 100 G transport networks," IEEE Commun. Mag. **48**(3), S48–S55 (2010).
44. O. Ozolins, L. Zhang, A. Udalcovs, *et al.*, "100 Gbaud PAM4 link without EDFA and post-equalization for optical interconnects," in *45th European Conference on Optical Communication (ECOC)* (IET, 2019), pp. 1–4.
45. A. Bogris, A. Argyris, and D. Syvridis, "Encryption efficiency analysis of chaotic communication systems based on photonic integrated chaotic circuits," IEEE J. Quantum Electron. **46**, 1421–1429 (2010).
46. P. Grassberger and I. Procaccia, "Measuring the strangeness of strange attractors," in *The Theory of Chaotic Attractors* (Springer, 2004), pp. 170–189.
47. A. Uchida, *Optical Communication with Chaotic Lasers: Applications of Nonlinear Dynamics and Synchronization* (Wiley, 2012).
48. O. Spitz, A. Herdt, W. Elsässer, *et al.*, "Stimulating polarization switching dynamics in mid-infrared quantum cascade lasers," J. Opt. Soc. Am. B **38**, B35–B39 (2021).
49. M. Yousefi, D. Lenstra, G. Vemuri, *et al.*, "Control of nonlinear dynamics of a semiconductor laser with filtered optical feedback," IEEE Proc. Optoelectron. **148**, 233–237 (2001).
50. M. Zhao, G. Xia, K. Yang, *et al.*, "Nonlinear dynamics of mid-infrared interband cascade lasers subject to variable-aperture optical feedback," Photonics **9**, 410 (2022).
51. Y. Liu and Y. Braiman, "Synchronization of high-power broad-area semiconductor lasers," IEEE J. Sel. Top. Quantum Electron. **10**, 1013–1024 (2004).
52. F. Grillot, A. Gavrielides, O. Spitz, *et al.*, "Talbot coupling of an array of quantum cascade lasers," Proc. SPIE **10540**, 224–231 (2018).
53. S. Koyu, O. Spitz, M. A. Berrill, *et al.*, "Dynamics and phase-locking in large heterogeneous arrays of semiconductor diode lasers," Proc. SPIE **12403**, 199–215 (2023).